Considering Nonsurface Scattering in Physical Optics Approximations

Orell Garten, *Graduate Student Member, IEEE*, Christoph Statz, *Graduate Student Member, IEEE*,
Steffen Gerling, Jochen Jebramcik, *Graduate Student Member, IEEE*, Jan Barowski, *Senior Member, IEEE*,
Dirk Plettemeier, *Senior Member, IEEE*, and Ilona Rolfes, *Member, IEEE*

Abstract—This work addresses the issue of volume scattering effects within the context of the physical optics (PO) approach. This decreases the modeling and computational effort to simulate scattering from complex material compositions. It is shown that there is a natural progression from the classical PO for perfect electric conductors over the PO for dielectric scatterers toward the proposed formulation. Four specializations of the general algorithm are presented to emphasize the versatility of this approach. Details regarding the implementation of the proposed examples are described. Results for each of the special cases are shown and compared to commercially available full-wave solvers of CST and FEKO.

Index Terms—Computational electromagnetics, electromagnetic propagation, electromagnetic reflection, numerical simulation.

I. INTRODUCTION

THE investigation of electromagnetic scattering of complex objects is widely used in many applications. Within the field of nondestructive testing, electromagnetic waves are used to inspect radomes [1]–[5] regarding their electric properties to ensure their quality for aeronautical and automotive applications. Furthermore, the characterization of materials with free-space setups [6]–[10] is important for mobile material characterization applications, which might be useful in emergency situations.

An important application is the monitoring of infrastructure and building conditions [11]–[16] for the early detection of possibly disastrous cracks that are buried inside the structure and, therefore, are not visible. Another application is geophysical remote sensing and ground-penetrating radar [17]–[22],

which is a tool in environmental monitoring, humanitarian missions, and space applications.

Many of these applications feature rather complicated media configurations with significant volume scattering.

To understand the scattering mechanisms and provide synthetic data for algorithm evaluation, fast simulation methods that calculate the scattered fields are extensively studied. One of the challenging problems is the large-scale nature of many of these problems while still maintaining an accurate representation of small-scale volume scattering effects.

Methods such as the finite-difference in time-domain (FDTD) [23] or the finite-element method (FEM) are well-suited for the simulation of the volume scattering. Although there are on-going developments to decrease the simulation times for large-scale scenarios, the overall time, memory, and power consumption of the FDTD are still too high in many cases [24]–[28]. The high computational complexity is mostly due to the volume discretization of the entire simulation domain, which is not reasonable for many propagation channel simulations.

In contrast, integral-based methods, such as the method of moments (MoM), are well-suited for such large-scale scattering problems because they discretize only the surface of the scatterer [29]. Unfortunately, inhomogeneous media within the simulation domain poses a problem for arbitrary scattering geometries because inhomogeneities are not covered by surface discretization. While discretizing the entire volume is possible, it drastically increases the computational cost and renders the method unfeasible for such scattering problems.

For special cases, such as planarly layered media, the free-space Green's function is replaced by Green's function for layered media [26], [30], [31].

A different way to compute the scattered fields is asymptotic simulation methods, such as the geometrical optics (GO) or physical optics (PO) approach. These are well-suited for the simulation of realistic, large-scale scenarios [32], [33]. While the GO is generally able to simulate volume effects that occur on scales much larger than the wavelength, it is not well-suited for small-scale volume scattering effects.

The PO approach is based on discretizing the surface of the scattering object and formulating equivalent current densities on each facet. These current densities are used as source terms within the integral equations to compute the backscattered
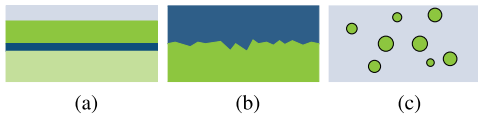
Fig. 1. Examples of complex media that exhibits significant volume scattering effects that cannot be neglected when simulating back scattered fields: (a) multilayer medium, (b) two-layer medium with rough interface, and (c) volume with inhomogeneous spots.

electromagnetic field. Due to the way the current densities are calculated, neither multiple bounces of the incident wave nor any volumetric scattering is considered by the PO. Therefore, each face at the surface of the scatterer can be considered independent during the computation, which increases the computational efficiency. On the other hand, it restricts the suitability of the algorithm for arbitrary scenarios. This approach has been applied successfully in many applications, e.g., astrophysical simulations [34]–[36] or in the design of military airplanes and ships [37]–[39].

One of the disadvantages of the PO compared to the FDTD or FEM is that it does not address any volume effects, which can have a significant impact on the overall scattering. There have been contributions to address this issue [7], [40], [41]. In [7] and [40], the main contribution is with respect to layered dielectrics, especially in combination with complex-shaped scattering bodies. Furthermore, Albani *et al.* [41] focus mostly on thin layers with arbitrary boundary conditions. Those approaches are quite useful but do not provide a general framework for arbitrary volume scattering effects.

Although the abovementioned simulation methods have many advantages, they are not well-suited for multiscale problems [29], [31], [42]. In recent years, a lot of work has been done to combine different methods, leading to so-called hybrid methods. Examples can be found in the literature [43]–[53]. It is noticeable that the goal of the hybridization is to find two or more conventional simulation methods that mitigate each other's disadvantages. This leads to very application-specific simulation methods. Their validity needs to be evaluated for each application.

This work tries to address the issue of hybridization of the PO method in a rather general way. With this method, it is straightforward to find new PO-based descriptions of scattering scenes, including different kinds of volume scattering. Examples for volume scattering, such as multilayer structures or materials with inclusions, are depicted in Fig. 1.

The structure of the work is given as follows: 1) we briefly review the PO approach for perfect electric conductors (PEC) and for dielectric bodies and 2) the main part of this work proposes a general way to address volume scattering in terms of a PO approach. Several examples will be shown, and implementation details are given. Before concluding, we validate our approach in a practical scenario.

II. PO AND FRANZ' FORMULAS

As usual, vectors are boldface letters. Complex-valued time-harmonic field vectors are capitalized and boldface as well. Matrices are double-overlined in order to hint at the

rank of the tensor. Complex-valued nonvector quantities are underlined.

A. Physical Optics

The PO approach is well-known in the literature and will only be reviewed very briefly. Interested readers are referred to [33]–[35], [39], [40], [54]–[56].

In general, the PO is based on the formulation of equivalent current densities based on the total fields at the interface of two materials. With the boundary conditions evaluated for PEC and the incident fields $\mathbf{E}^{\text{inc}}$ and $\mathbf{H}^{\text{inc}}$, this leads to

$$\mathbf{J}(\mathbf{r}) = 2\hat{\mathbf{n}}(\mathbf{r}) \times \mathbf{H}^{\text{inc}}(\mathbf{r}) \tag{1}$$

$$\mathbf{M}(\mathbf{r}) = 0, \tag{2}$$

where $\mathbf{J}(\mathbf{r})$ is the electric and $\mathbf{M}(\mathbf{r})$ the magnetic current density on the surface of the scattering object. The unit normal vector $\hat{\mathbf{n}}(\mathbf{r})$ on the surface is location-dependent. Within the rest of this article, this location-dependence will be implicit and not shown in the notation for the sake of conciseness.

The formulation in (1) and (2) only holds for PEC bodies. In many practical cases, dielectric scatterers are present in the simulation domain [54], [8], and [18]. Therefore, the PO has been extended toward penetrable bodies in [36], [57], and [34]. Different formulations for the electric and magnetic current densities $\mathbf{J}_{\text{pen}}$ and $\mathbf{M}_{\text{pen}}$ are available in the previously mentioned literature. We choose to implement

$$\mathbf{J}_{\text{pen}} = \hat{\mathbf{n}} \times [(1 - \Gamma_\perp)\overline{\overline{\mathbf{P}}}_\perp + (1 - \Gamma_\parallel)\overline{\overline{\mathbf{P}}}_\parallel] \cdot \mathbf{H}^{\text{inc}} \tag{3}$$

$$\mathbf{M}_{\text{pen}} = -\hat{\mathbf{n}} \times [(1 + \Gamma_\perp)\overline{\overline{\mathbf{P}}}_\perp + (1 + \Gamma_\parallel)\overline{\overline{\mathbf{P}}}_\parallel] \cdot \mathbf{E}^{\text{inc}} \tag{4}$$

from [35] due to its straightforward implementation.

The local reflection coefficients $\Gamma_\perp$ and $\Gamma_\parallel$ are introduced by enforcing the boundary conditions on the surface. They are equivalent to the Fresnel coefficients. The matrices $\overline{\overline{\mathbf{P}}}_\parallel$ and $\overline{\overline{\mathbf{P}}}_\perp$ describe the projection of the electromagnetic field onto the perpendicular and parallel unit vector, respectively. Their purpose is to split the impinging wave into its spatially orthogonal components. The definition is given as follows:

$$\overline{\overline{\mathbf{P}}}_\parallel = \mathbf{e}_\parallel \otimes \mathbf{e}_\parallel \tag{5}$$

$$\overline{\overline{\mathbf{P}}}_\perp = \mathbf{e}_\perp \otimes \mathbf{e}_\perp \tag{6}$$

$$\overline{\overline{\mathbf{P}}}_\parallel, \overline{\overline{\mathbf{P}}}_\perp \in \mathbb{R}^{3 \times 3} \tag{7}$$

where $\otimes$ denotes the outer product and $\mathbf{e}_\parallel$ and $\mathbf{e}_\perp$ the parallel and perpendicular unit vectors, respectively. The advantage of this formulation is that it allows dealing with sources polarized in an arbitrary way. Therefore, it is highly suitable for realistic simulations with realistic antenna models.

B. Franz' Formulas

Franz' Formulas, such as the wildly used Stratton–Chu formulas, are integral equations used to calculate the electric and magnetic field resulting from the surface current densities $\mathbf{M}$ and $\mathbf{J}$. [58], [59]. However, the Stratton–Chu formulas cannot cover discontinuities in the surface current densities.

Typically, we are only interested in the far-field approximations for the scattered fields. Due to the uniqueness theorem

[33, p. 314], only the tangential components of either the electric or the magnetic field need to be known on the surface to uniquely represent the scattered far-field. Then, the far-field approximations are given as

$$\mathbf{E}(\mathbf{r}) \simeq J\underline{k} \iint_{S'} g_0(\mathbf{r}, \mathbf{r}') \cdot \frac{\mathbf{r} - \mathbf{r}'}{|\mathbf{r} - \mathbf{r}'|} \times \mathbf{M}_S(\mathbf{r}') \, \mathrm{d}S' \quad (8)$$

$$\mathbf{H}(\mathbf{r}) \simeq -J\underline{k} \iint_{S'} g_0(\mathbf{r}, \mathbf{r}') \cdot \frac{\mathbf{r} - \mathbf{r}'}{|\mathbf{r} - \mathbf{r}'|} \times \mathbf{J}_S(\mathbf{r}') \, \mathrm{d}S' \quad (9)$$

where $\mathbf{E}$ and $\mathbf{H}$ are the fields only due to the surface current densities $\mathbf{M}$ and $\mathbf{J}$ in the source region S'. The scalar free-space Green's function is denoted by g_0, and $\underline{k}$ is the complex wavenumber.

Theoretically, Franz' formulas are advantageous compared to Stratton–Chu equations [60] when dealing with discontinuous current distributions on a surface, which are typically encountered in PO computations [58], [59]. In the far-field formulation, the Stratton–Chu equations are identical to Franz' formulas.

III. ALGORITHM

The theory reviewed in Section II will now be extended toward scattering from objects with significant volume scattering. The goal is to find a formulation similar to the conventional PO, which allows us to include such volume scattering effects. For the traditional PO approach, surface current densities are calculated to describe the scattered field. In this extension, we calculate surface current densities as well; however, they need to describe the volumetric behavior of the scattering object.

Therefore, we modify (3) and (4) such that

$$\mathbf{J}_{\mathrm{tot}} = \hat{\mathbf{n}} \times [(1 - \Gamma_{0,\perp}) \cdot \overline{\overline{\mathbf{P}}}_\perp + (1 - \Gamma_{0,\parallel}) \cdot \overline{\overline{\mathbf{P}}}_\parallel] \cdot \mathbf{H}^{\mathrm{inc}}$$
$$+ \hat{\mathbf{n}} \times [\mathcal{C}_\perp^{\mathbf{J}}(\overline{\overline{\mathbf{P}}}_\perp \cdot \mathbf{H}^{\mathrm{inc}}) + \mathcal{C}_\parallel^{\mathbf{J}}(\overline{\overline{\mathbf{P}}}_\parallel \cdot \mathbf{H}^{\mathrm{inc}})] \quad (10)$$

$$\mathbf{M}_{\mathrm{tot}} = -\hat{\mathbf{n}} \times [(1 + \Gamma_{0,\perp}) \cdot \overline{\overline{\mathbf{P}}}_\perp + (1 + \Gamma_{0,\parallel}) \cdot \overline{\overline{\mathbf{P}}}_\parallel] \cdot \mathbf{E}^{\mathrm{inc}}$$
$$- \hat{\mathbf{n}} \times [\mathcal{C}_\perp^{\mathbf{M}}(\overline{\overline{\mathbf{P}}}_\perp \cdot \mathbf{E}^{\mathrm{inc}}) + \mathcal{C}_\parallel^{\mathbf{M}}(\overline{\overline{\mathbf{P}}}_\parallel \cdot \mathbf{E}^{\mathrm{inc}})] \quad (11)$$

where $\mathcal{C}^{\mathbf{J}}(\overline{\overline{\mathbf{P}}}_\perp \cdot \mathbf{H}^{\mathrm{inc}})$, $\mathcal{C}^{\mathbf{J}}(\overline{\overline{\mathbf{P}}}_\parallel \cdot \mathbf{H}^{\mathrm{inc}})$, $\mathcal{C}^{\mathbf{M}}(\overline{\overline{\mathbf{P}}}_\perp \cdot \mathbf{E}^{\mathrm{inc}})$, and $\mathcal{C}^{\mathbf{M}}(\overline{\overline{\mathbf{P}}}_\parallel \cdot \mathbf{E}^{\mathrm{inc}})$ describe the additional contributions of the volume for electric and magnetic current densities, respectively. The indices $\perp$ and $\parallel$ stand for perpendicular and parallel polarization. Compared to the traditional formulation, we introduce $\mathcal{C}_{\perp,\parallel}^{\mathbf{J}}$ and $\mathcal{C}_{\perp,\parallel}^{\mathbf{M}}$ to describe the volume scattering of the medium for perpendicular and parallel polarizations, respectively. These terms can be interpreted as projectors of the volume scattering to the surface currents. They can be defined rather freely to describe the medium, which we will see in Sections III-A–III-C. To demonstrate the versatility and applicability of the approach, Sections III-A–III-C show three different choices for $\mathcal{C}_{\perp,\parallel}^{\mathbf{J}}$ and $\mathcal{C}_{\perp,\parallel}^{\mathbf{M}}$.

A. Dielectric Slab With Born Approximation

A dielectric slab is the easiest possible scenario for a multilayer medium because it consists of only two different media. The first layer has a finite thickness and is followed by a dielectric half-space with arbitrary properties. Under the

assumption of the first-order Born approximation, therefore neglecting multiple reflections within the medium, we find the terms $\mathcal{C}_\perp^{\mathbf{J}}, \mathcal{C}_\parallel^{\mathbf{J}}, \mathcal{C}_\perp^{\mathbf{M}}$, and $\mathcal{C}_\parallel^{\mathbf{M}}$ as

$$\mathcal{C}_{\perp,\parallel}^{\mathbf{J}}(\mathbf{H}^{\mathrm{inc}}) = (1 - \Gamma_{1,\perp,\parallel}) \cdot T_{\perp,\parallel}^{10} \cdot T_{\perp,\parallel}^{01}$$
$$\cdot e^{-2J \cdot \underline{k}_1 \cdot d_1} \cdot (\overline{\overline{\mathbf{P}}}_{\perp,\parallel} \cdot \mathbf{H}^{\mathrm{inc}}), \quad (12)$$

$$\mathcal{C}_{\perp,\parallel}^{\mathbf{M}}(\mathbf{E}^{\mathrm{inc}}) = (1 + \Gamma_{1,\perp,\parallel}) \cdot T_{\perp,\parallel}^{10} \cdot T_{\perp,\parallel}^{01}$$
$$\cdot e^{-2J \cdot \underline{k}_1 \cdot d_1} \cdot (\overline{\overline{\mathbf{P}}}_{\perp,\parallel} \cdot \mathbf{E}^{\mathrm{inc}}) \quad (13)$$

where $\Gamma_{1,\perp,\parallel}$ is the reflection coefficient at the back surface and $T_{\perp,\parallel}^{10}$ and $T_{\perp,\parallel}^{01}$ are the transmission coefficients from free space into the slab and vice versa for both polarizations. The distance d_1 is the actual path length of the wave traveled within the slab, which is not to be confused with the slab thickness.

To extend this method toward multilayer structures, the reflection coefficient $\Gamma_{1,\perp,\parallel}$ needs to be adapted to include the effects of the medium behind the layer as well. Basically, this allows a recursion to simulate multilayer scenarios.

Since this assumes the first-order Born approximation to hold, we conclude that this formulation is only valid for relatively weak contrasts or for cases where multiple reflections are irrelevant for the desired application.

B. Dielectric Slab Including Internal Reflections

The aforementioned considerations do not consider any multiple reflections within the medium; however, in many practical cases, e.g., material characterization, this is not a valid assumption [7], [8]. The following is a straighforward extension of recent works [7], [61]. For stronger contrasts, we need to model the nonnegligible multiple reflections within the medium as well. This changes the terms (12) and (13) to

$$\mathcal{C}_{\perp,\parallel}^{\mathbf{J}}(\mathbf{H}^{\mathrm{inc}})$$
$$= \frac{(\Gamma_{0,\perp,\parallel}^2 - 1) \cdot \Gamma_{1,\perp,\parallel} \cdot e^{-2J \cdot \underline{k}_1 \cdot d_1}}{1 + \Gamma_{0,\perp,\parallel} \cdot \Gamma_{1,\perp,\parallel} \cdot e^{-2J \cdot \underline{k}_1 \cdot d_1}} \cdot (\overline{\overline{\mathbf{P}}}_{\perp,\parallel} \cdot \mathbf{H}^{\mathrm{inc}}) \quad (14)$$

$$\mathcal{C}_{\perp,\parallel}^{\mathbf{M}}(\mathbf{E}^{\mathrm{inc}})$$
$$= \frac{(1 - \Gamma_{0,\perp,\parallel}^2) \cdot \Gamma_{1,\perp,\parallel} \cdot e^{-2J \cdot \underline{k}_1 \cdot d_1}}{1 + \Gamma_{0,\perp,\parallel} \cdot \Gamma_{1,\perp,\parallel} \cdot e^{-2J \cdot \underline{k}_1 \cdot d_1}} \cdot (\overline{\overline{\mathbf{P}}}_{\perp,\parallel} \cdot \mathbf{E}^{\mathrm{inc}}) \quad (15)$$

where $\Gamma_{0,\perp}$, $\Gamma_{1,\perp}$, $\Gamma_{0,\parallel}$, and $\Gamma_{1,\parallel}$ are the reflection coefficients at the first and second interfaces. For a dielectric slab, they are equivalent to the local reflection coefficient. When considering multilayer media, the reflections coefficients $\Gamma_{1,\perp}$ and $\Gamma_{1,\parallel}$ need to describe the multilayer behavior as well. The exponential in (14) and (15) describes the phase shift, which is due to the thickness of the layer. For oblique incidence, the length d_1 describes the actual distance the wave travels within the medium. Technically, this is the reflection coefficient of a slab, including all multiple reflections; however, the surface reflection is not included because this is already covered in the regular PO part of (10) and (11).

Contrary to the model before, this approach will also be valid for stronger contrasts because multiple reflections within the medium are considered. This example already shows how different aspects of the scattering mechanism can be included in the model in a consistent manner. This emphasizes the flexibility of the proposed algorithm.
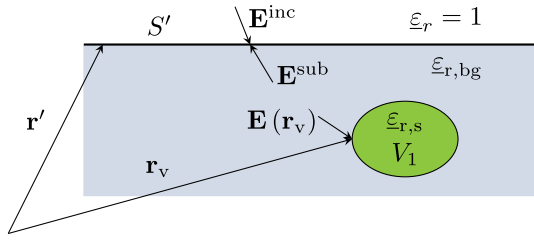
Fig. 2. Model for the algorithm to simulate backscattering from dielectric media with inclusions. $\mathbf{E}^{\text{inc}}$ is the incident wave on the volume V, which contains a region V_1 that has a permittivity different from the background medium with an impinging wave $\mathbf{E}(\mathbf{r}_{\text{v}})$. The vector $\mathbf{r}_{\text{v}}$ describes the entire volume; however, the volumetric integration only contributes for $\mathbf{r}_{\text{v}} \in V_1$. This results in the electric field $\mathbf{E}^{\text{sub}}$ on the inside of the dielectric bodies bounding surface S' described by $\mathbf{r}'$.

C. Dielectric Medium With Inclusions

This part shows how an existing method described in [54] can be expressed in terms of the newly proposed algorithm. The algorithm [54] deals with arbitrarily shaped weak inhomogeneities in the volume V, which is bounded by its surface S'. The problem formulation is depicted in Fig. 2 where the inhomogeneity is denoted by V_1. Note that, for arbitrary cases, the inhomogeneous regions can be disjoint, e.g., as depicted in Fig. 1(c).

Generally, the operators $\mathcal{C}_{\perp,\|}^{\mathbf{M}}$ and $\mathcal{C}_{\perp,\|}^{\mathbf{J}}$ describe the contribution of the volume scattering to the overall scattered field. In the following, we will derive $\mathcal{C}_{\perp,\|}^{\mathbf{M}}$ in terms of the incident electric field. A graphical representation of the following quantities is shown in Fig. 2. The volumetric scattering contribution can be expressed by

$$\mathcal{C}_{\perp,\|}^{\mathbf{M}}(\mathbf{E}^{\text{inc}}) = \left(1 + \Gamma_{\perp,\|}^{01}\right)\mathbf{E}^{\text{sub}}(\mathbf{F}_{\perp,\|}(\mathbf{E}^{\text{inc}})) \qquad (16)$$

where Γ^{ij} determines the Fresnel reflection coefficient for wave incidence in medium j, $\mathbf{E}_{\perp,\|}^{\text{sub}}$ is the electric field impinging on the inside of S' from within the volume, and $\mathbf{E}^{\text{inc}}$ is the primary incident field. $\mathbf{F}_{\perp,\|}$ describes the perpendicular and parallel components of the incident electric field

$$\mathbf{F}_{\perp,\|}(\mathbf{E}^{\text{inc}}) = \overline{\overline{\mathbf{P}}}_{\perp,\|} \cdot \mathbf{E}^{\text{inc}}. \qquad (17)$$

Next, the electric field $\mathbf{E}_{\perp,\|}^{\text{sub}}$ needs to be computed. Note that the scattered field is dependent on the incident field at the surface, the constitutive parameters of the background material, and the contrast function

$$\underline{\chi}(\mathbf{r}_{\text{v}}) = \underline{\varepsilon}_{\text{r,s}}(\mathbf{r}_{\text{v}}) - \underline{\varepsilon}_{\text{r,bg}} \qquad (18)$$

which describes the inhomogeneity of the volume in terms of the relative permittivities of the background and the inclusions. This follows the notation in [62]. Furthermore, within the medium, we assume that the first-order Born approximation holds, and therefore, the electric field due to scattering within the volume can be computed by

$$\mathbf{E}^{\text{sub}}(\mathbf{F}_{\perp,\|}) = \iiint_V g_0(\mathbf{r}_{\text{v}}, \mathbf{r}') \cdot \underline{\chi}(\mathbf{r}_{\text{v}}) \cdot \mathbf{E}(\mathbf{r}_{\text{v}}, \mathbf{F}_{\perp,\|}) \, dV \qquad (19)$$

where g_0 is the Greens function of a point source in the background medium. The integration domain V spans the entire volume; however, only regions where $\underline{\chi} \neq 0$ contribute

to the scattered field. Using (19) results in the following consequences.

1) Multiple reflections within the medium are not considered.
2) Large inclusions will contribute to the scattered field at all points even though, realistically, only the boundary will add to the scattered field.

For media with weak inhomogeneities, these two limitations do not invalidate the method.

Finally, the incident electric field $\mathbf{E}_{\perp,\|}(\mathbf{r}_{\text{v}}, \mathbf{F})$ at the inclusion is calculated with Franz' formula

$$\mathbf{E}(\mathbf{r}_{\text{v}}, \mathbf{F}_{\perp,\|}) = j\underline{k} \iint_{S'} g_0(\mathbf{r}', \mathbf{r}_{\text{v}}) \cdot \frac{\mathbf{r}' - \mathbf{r}_{\text{v}}}{|\mathbf{r}' - \mathbf{r}_{\text{v}}|}$$
$$\times \left[\hat{\mathbf{n}} \times \left(1 + \Gamma_{\perp,\|}^{10}\right)\mathbf{F}_{\perp,\|}(\mathbf{r}')\right] dS'. \qquad (20)$$

The term $\hat{\mathbf{n}} \times (1 + \Gamma_{\perp,\|}^{10})\mathbf{F}$ describes the source current of the electric field and is equivalent to $-\mathbf{M}_S(\mathbf{r}')$. Analogously, this can be done with the magnetic field, as well by changing $1 + \Gamma_{\perp,\|}$ to $1 - \Gamma_{\perp,\|}$.

The formulation derived in Section III-C is rather complicated and computationally expensive due to the fact that multiple integrals have to be solved; however, compared to the formulations in Sections III-A and III-B, this method is rather general.

IV. IMPLEMENTATION

The implementation of the method is done within a ray-based simulation framework, which is based on *Intel*'s Embree library [63] for efficient ray tracing, which provides efficient ray tracing kernels (e.g., ray-surface-intersection testing). For the PO, rays are traced until they reach the first surface where the surface current densities are calculated. Essentially, ray tracing is used to discriminate between lit and nonlit areas of the scatterer's surface and to discretize the surface of scatterers.

The rays are launched in an equiangular manner around the source location, and they are used to discretize the scattering object generating N surface facets. This has the advantage that each ray has the same share of the spherical surface around the source, which leads to a surface element within the integration steps that are only dependent on the distance from the source.

Next, the equations in Section III are applied to each surface facet on the scattering object. The computation of the integrals is done by applying zeroth-order approximations, hence using point-matching and stationary-phase assumptions for each facet.

For each launched ray, we define a matrix $\overline{\overline{\mathbf{T}}}$, which describes the projection of the source field $\mathbf{E}_{\text{inc}}$ onto the observed field $\mathbf{E}_{\text{obs}}$ [54]

$$\mathbf{E}_{\text{obs}} = \overline{\overline{\mathbf{T}}} \cdot \mathbf{E}_{\text{inc}}. \qquad (21)$$

All cross products during the computation are substituted by their equivalent matrix representations, which leads to an overall transmission matrix $\overline{\overline{\mathbf{T}}}$, as shown in (21).

This approach has the advantage that the antenna pattern does not have to be known during the simulation and can be added in an additional postprocessing step [64]. This is

especially useful in practical applications, e.g., when designing and optimizing experiments regarding the antenna.

The general simulation procedure is shown in Algorithm 1. First, intersections of all launched rays with the scattering scene are calculated via path tracing. Frequency-independent data, such as geometric path lengths, are stored during this phase. Next, for each frequency of interest, we loop over all launched rays and calculate the transmission from the source to the surface facet, then calculate the corresponding frequency-dependent electric and magnetic current densities, and, finally, compute the observed field at the receiver according to (8) and (9). Eventually, we calculate $\underline{S}_{11}$, as proposed in [64], for each frequency. To obtain the time-domain response, we Fourier transform the frequency response.

Algorithm 1 General Algorithm to Simulate Scattered Fields

---

for all rays **do**
    calculate intersections with geometry
    save frequency independent data
end for
for all frequencies **do**   ▷ (*)
    for all rays **do**   ▷ (#)
        calculate transmission to this surface facet
        calculate current densities with (10) and (11)   ▷ (+)
        calculate observed field $\mathbf{E}_{\text{obs}}$ with (21)
    end for
    calculate $\underline{S}_{11}$ as proposed in [64]
end for

To decrease the simulation time, we can parallelize the algorithm for the frequency loop (∗) or for the loop traversing the rays (#). Most straightforward is the parallelization of the inner loop (#) because no elaborate data access needs to be implemented.

The novelty, compared to other approaches, lies in step (+) when the volume effects are computed.

V. RESULTS

A. Reference Results

For the validation of the three algorithms given in Section III, reference simulations have been made. We show examples of a one-layer dielectric, a two-layer dielectric, and a medium with inhomogeneous inclusion.

For the first two examples of layered dielectrics, we have simulated realistic scenarios, including the excitation via a lens antenna similar to [65] with the finite integration technique (FIT) of CST Microwave Studio 2019 [66].

Unfortunately, the FIT suffers from discretization effects, which can lead to a small time shift of the peaks in the time-domain responses even for very fine meshing. Numerical experiments have shown that a discretization of about $\lambda/18$ needs to be chosen for the cell size of the FIT grid for our case; however, this leads to very time- and memory-consuming simulations that can only be computed on a dedicated server. The reference results for the case III-C have been simulated with plane wave excitation in FEKO [67]. This plane wave assumption is valid for scenarios where the scatterer is far
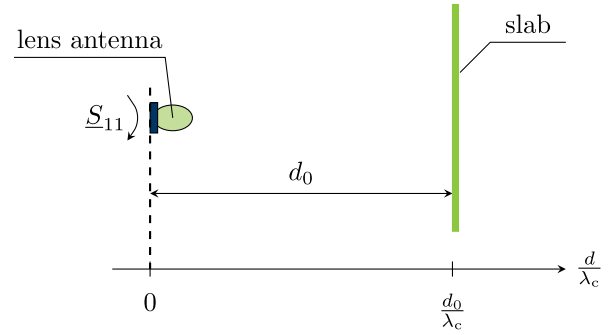

Fig. 3. Setup for the simulations according to Sections III-A and III-B. For the two-layer setup, the slab is replaced by two dielectric slabs. The simulations are done with a realistic antenna model, which is located at a distance d_0 from the slab.

away from the antenna and the effect of the variations in the medium is locally confined. Technically, this assumption is stronger than a simple far-field assumption because the wave needs to be considered a plane wave over the entire simulation domain.

FEKO implements the method of moments (MoM), an integral solver, to compute the scattered field. Since the free space does not need to be meshed, this is rather efficient for large-scale scattering problems if the scatterer is homogeneous. In our scenario, the scatterer is modeled as a dielectric half-space, which can be dealt with efficiently in the MoM via the Sommerfeld integral. The inclusions are modeled as spheres within this half-space.

B. Simulation Results

1) Dielectric Slab: The first reference scenario is a dielectric slab embedded in a free-space environment, which is a rather simple scattering scenario. The slab has a thickness of $t_{\text{slab}} = 30$ mm, which is roughly equivalent to seven free-space wavelengths λ_{c} at the center frequency $f_{\text{c}} = 80$ GHz.

Because the slab is embedded in free space, the relative background permittivity is $\underline{\varepsilon}_{\text{r,bg}} = 1$. The permittivity of the slab is varied and is chosen to be $\underline{\varepsilon}_{\text{r,s}} \in \{1.2; 3.2\}$ to verify the behavior with a small and stronger contrast. The general setup of the simulation is shown in Fig. 3. The primary source is the precomputed field of a lens antenna, which is located at a distance $d_0/\lambda_{\text{c}} = 106$ from the slab.

The simulation results for both contrasts are depicted in Fig. 4. It includes the PO without internal multiple reflections according to III-A and the PO modeling the multiple reflections according to III-B. The reference simulation method is the FIT in CST. The abscissae are normalized on the free-space center wavelength λ_{c}. This leads to the fact that the reflections from inside the medium appear to be farther away because the distance calculation assumes that the wave travels with c_0, the speed of light in free space

$$\frac{d'}{\lambda_{\text{c}}} = f_{\text{c}} \cdot \frac{t}{2} \quad \forall t \tag{22}$$

where t is the round-trip time from the source to a point in distance d and back to the source. If a material is present,
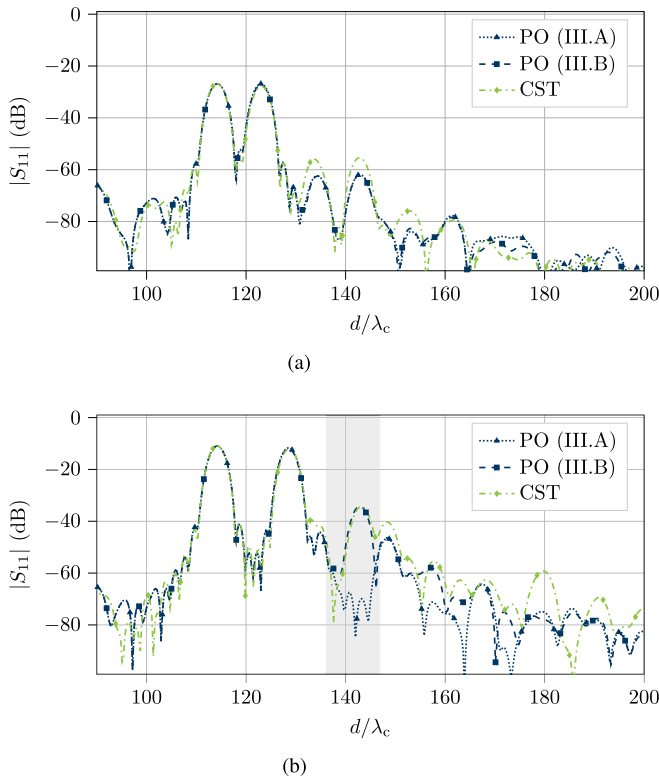
(a)

(b)

Fig. 4. Time-domain response of the CST and PO Simulations for a one-layer dielectric. Two main peaks are clearly visible in both plots. For a difference of $\chi = 0.2$, all methods match quite well. For a stronger contrast, the PO that does not model multiple reflections shows different behaviors in the gray area. The PO (III-B) matches the full-wave CST simulation quite well. (a) $\underline{\chi} = 0.2$. (b) $\underline{\chi} = 2.2$.

the propagation velocity of the wave is a factor $1/\sqrt{\varepsilon}$ smaller than in free space. Therefore, the peak on the axis appears to be later than expected and needs to corrected for when evaluating this distance by subtracting

$$\frac{\Delta d}{\lambda_{\mathrm{c}}} = \frac{f_{\mathrm{c}}}{\sqrt{\varepsilon_{\mathrm{r,2}}}} \cdot \frac{\Delta t}{2} \tag{23}$$

from the distance on the abcissae. In (23), $\underline{\varepsilon}_{\mathrm{r,2}}$ is the relative permittivity of the medium and Δt the round trip time of the wave within the medium.

The time-domain response in Fig. 4 exhibits two main peaks that are equal in all three methods; however, the first peak is slightly later than expected from the theory. This is due to the fact that the speed of light within the antenna is not equal to the vacuum speed of light, which is used to calculate the values on the abscissae.

It can clearly be seen that the time-domain response in Fig. 4(a) of all three methods matches quite well for a relatively small contrast of $\underline{\chi} = 0.2$ because multiple reflections are negligible for weak contrasts. However, amplitude deviations are visible for the peaks at $d/\lambda_{\mathrm{c}} = 135$ and $d/\lambda_{\mathrm{c}} = 145$. These peaks are due to the multiple reflections within the lens antenna [65], which are underestimated in the approach of [64]. In Fig. 4(b), strong differences are visible in the grayly marked area. These differences are mainly due to
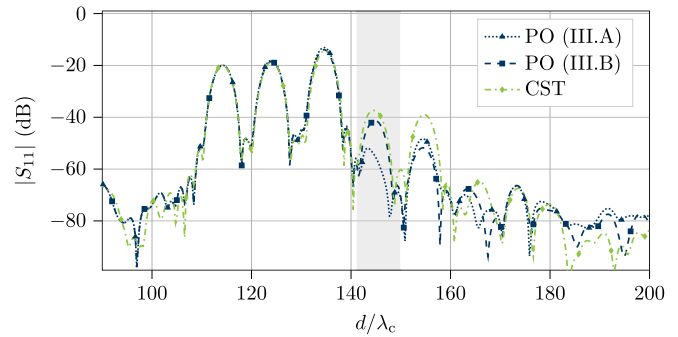
Fig. 5. Time-domain response of the CST and PO simulations for a two-layer medium. The three main reflections resulting from the three material interfaces agree quite well between all methods. The PO (III-A) method does not model the multiple reflections occurring in the gray overlay. Nevertheless, the PO (III.B) agrees well with the CST simulation, and it is clearly shown how multiple reflections are considered as well.

the multiple reflections within the medium. This is the result we expected from the theory in III-A and III-B.

2) Two-Layer Dielectric Medium: The reference simulation for the two-layer dielectric is done equivalently to the simulations for the dielectric slab. The setup in Fig. 3 is still valid; however, the slab is replaced by a medium with two layers with the relative permittivities $\underline{\varepsilon}_{\mathrm{r,1}} = 1.5$ and $\underline{\varepsilon}_{\mathrm{r,2}} = 2.5$. The simulation results are shown in Fig. 5. The graph denoted as PO (III.A) depicts the simulation without internal multiple reflections, which is a direct continuation of III-A toward two-layer media [7]. The simulation including internal multiple reflections within the medium is labeled as PO (III.B).

Three distinct peaks are visible in the time-domain response that corresponds to the three material interfaces. The first peak appears slightly later than expected, which is due to the above-mentioned reasoning. The area with the gray overlay in Fig. 5 corresponds to the internal reflections in the two-layer medium. Again, the PO (III.A) did not model these reflections. The small amplitude difference between the reference simulation and PO (III.B) is again due to the underestimation of the multiple reflections in the antenna itself. This effect can also be seen in the last major peak at $d/\lambda_{\mathrm{c}} \approx 155$.

3) Inclusions in Dielectric Half-Space: The reference data for the third example were generated using FEKO. Instead of a realistic antenna model, we use a plane wave excitation in free space. The background material is considered to be a dielectric half-space with a relative permittivity of $\underline{\varepsilon}_{\mathrm{r}} = 2$. The inclusion used in this example is a dielectric sphere. Results for two different contrasts $\underline{\chi}$ to the background medium are shown: first, a relatively weak contrast $\underline{\chi} = 0.01$; second, a stronger contrast with $\underline{\chi} = 0.2$. The input scattering parameter is calculated by using the approach in [64], assuming perfect input and output matching. This corresponds to a perfectly matched antenna where the scattering object is located far away from the antenna.

A schematic of the simulation scenario is shown in Fig. 6. Since the plane wave excitation fulfills the far-field assumption by definition, we only use a small distance between the
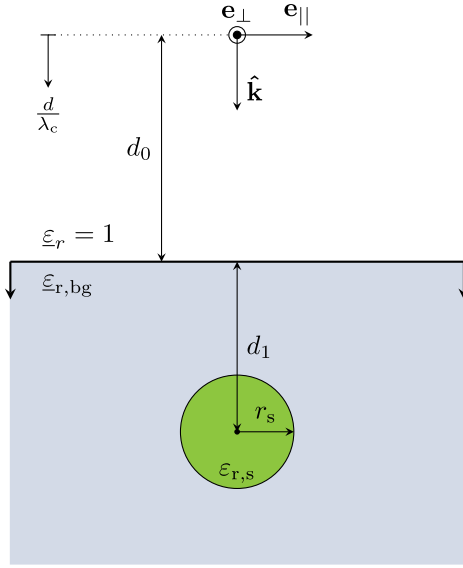
Fig. 6.   Simulation model for the extension proposed in Section III-C. A plane wave excitation of the scene is chosen to minimize the calculation time of the full-wave commercial solver. A dielectric sphere is included within a background medium, which is modeled as a dielectric half-space.
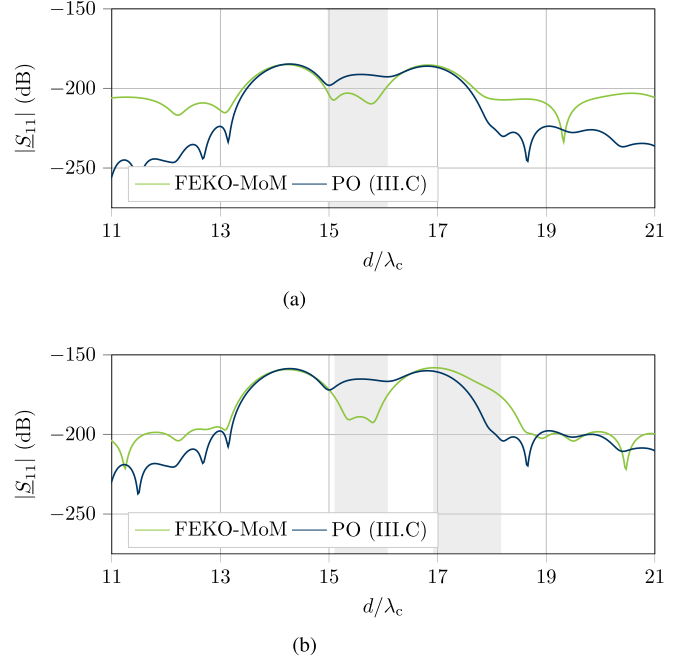

Fig. 7.   Relevant section of the time-domain response showing the volume scattering effects only. For a very weak contrast of $\chi = 0.01$, the responses match quite well for the interface reflections. Within the gray overlay, there are some differences. For a stronger contrast of $\chi = 0.2$, the differences for the region within the sphere are stronger. Furthermore, the reflection from the bottom of the sphere is different, and there are some differences. For a stronger contrast of $\chi = 0.2$, the differences for the region within the sphere are stronger. Furthermore, the reflection from the bottom of the sphere is different as well. (a) $\chi = 0.01$. (b) $\chi = 0.2$.

imaginary plane wave source point and the surface of the scatterer of $d_0/\lambda_c = 9.1$. The distance between the surface and the spherical scatterer is $d_1/\lambda_c = 4.55$. The radius of the sphere is $r_s/\lambda_c = 1$. The background permittivity of the half-space is $\underline{\varepsilon}_{r,bg} = 2$.

Fig. 7 shows the part of the time-domain response for two different contrasts $\underline{\chi}$, which is relevant to the reflection from the inclusion in the dielectric material. For both simulations, only the scattering due to the volume effects is presented since this is the relevant part for this work. The distance axis of the time-domain response is normalized on the wavelength of the center frequency. As a result of the dimensions of the problem, we expect reflections originating from the sphere at

$$\frac{d'}{\lambda_c} = \frac{d_0}{\lambda_c} + \left(\frac{d_1}{\lambda_c} - \frac{r_s}{\lambda_c}\right) \cdot \sqrt{\underline{\varepsilon}_{r,bg}} = 14.12 \qquad (24)$$

$$\frac{d''}{\lambda_c} = \frac{d_0}{\lambda_c} + \left(\frac{d_1}{\lambda_c} - \frac{r_s}{\lambda_c}\right) \cdot \sqrt{\underline{\varepsilon}_{r,bg}}$$
$$+ \frac{2 \cdot r_s}{\lambda_c} \cdot \sqrt{\underline{\varepsilon}_{r,s}}$$
$$\in \{16.96; 17.09\}. \qquad (25)$$

The first reflections in Fig. 7(a) and (b) match the theoretical values quite well; however, the location of the second reflection shows some deviations, especially for $\underline{\chi} = 0.2$. This is explained by the fact that the first-order Born approximation assumes that the wave traverses the sphere almost undisturbed. However, this assumption does not hold for stronger contrasts. Therefore, we expect a reflection at

$$\frac{\tilde{d}''}{\lambda_c} = \frac{d_0}{\lambda_c} + \left(\frac{d_1}{\lambda_c} + \frac{r_s}{\lambda_c}\right) \cdot \sqrt{\underline{\varepsilon}_{r,bg}} = 16.95 \qquad (26)$$

which is close to the location shown in Fig. 7(b). It is also noticeable that (26) is almost identical to the first result in (25).

This demonstrates the suitability of this method for weak contrasts.

The gray areas in Fig. 7(a) and (b) mark the regions of the time-domain response where the deviations between the reference simulation and the PO simulation are strong.

The advantage of this approach is its flexibility in modeling small inclusions within the material when the contrast between the background medium and the inclusions is small. For media where the Born approximation does not hold, different approaches, e.g., a more generalized Born approximation, such as [68], can be used; however, the computational effort will increase as well.

VI. CONCLUSION

Starting at the classical PO formulation, this article presents a novel general formulation to include rather arbitrary volume scattering effects within a PO framework. This is highly advantageous due to the fact that a PO method is faster than a full-wave simulation, such as the FIT or MoM. Therefore, this approach will decrease the time of planning experiments and systems based on such simulations. Moreover, it will allow algorithm evaluation with very well-defined volumetric scattering effects. This allows designers to study the behavior of their algorithms in a detailed way. Furthermore, high comparability between different models is given because only the calculation kernel for the volume scattering differs, while the rest of the calculation does not change.

Furthermore, we have shown that this step is a logical progression of the well-known PO formulations for PEC and homogeneous dielectric scatterers. The usefulness is illustrated with examples of varying complexity:

1) dielectric slab (Born approximation & multiple reflections);
2) two-layer medium;
3) arbitrarily shaped inhomogeneity.

These special cases are validated against full-wave reference simulations. It has been shown that each of the methods works well for the assumptions that were covered during the modeling phase. The PO is computationally much more efficient than the FIT of CST and MoM of FEKO, which both need to run on dedicated computing servers with many cores. Contrary to that, the proposed PO method runs on commercial laptop computers with only one core used for the computation. The limitation for the PO arises from the availability of enough random access memory (RAM) in order to store all the information needed for the simulations.

This work has also shown how such hybrid methods are application-specific and need to be evaluated for each case. Generally, it is possible to model all occurring effects when increasing computational cost is acceptable.

Concluding, this work offers a framework to address volume scattering issues of different complexity in the context of a PO approach.

REFERENCES

[1] M. Bauer *et al.*, "Volume inspection of composite structures in aircraft radomes with FMCW terahertz radar at 100 and 150 GHz," in *Proc. 43rd Int. Conf. Infr., Millim., THz Waves (IRMMW-THz)*, Sep. 2018, pp. 1–3.

[2] Q. Wang, X. Li, Y. Huang, H. Zhou, and Q. Hu, "Simulation study on nondestructive evaluation of glass fiber reinforced polymer with sandwich structure of radome by terahertz," in *Proc. 2nd IEEE Adv. Inf. Manage., Communicates, Electron. Autom. Control Conf. (IMCEC)*, May 2018, pp. 2436–2442.

[3] F. Friederich *et al.*, "Terahertz radome inspection," *Photonics*, vol. 5, no. 1, p. 1, Jan. 2018.

[4] J. Helander, A. Ericsson, D. Sjoberg, M. Gustafsson, T. Martin, and C. Larsson, "60 GHz imaging of panels for defect detection using planar scanning," in *Proc. IEEE Int. Symp. Antennas Propag. (APSURSI)*, Jun. 2016, pp. 1025–1026.

[5] K. Persson, M. Gustafsson, G. Kristensson, and B. Widenberg, "Radome diagnostics—Source reconstruction of phase objects with an equivalent currents approach," *IEEE Trans. Antennas Propag.*, vol. 62, no. 4, pp. 2041–2051, Apr. 2014.

[6] J. Jebramcik, J. Barowski, J. Wagner, and I. Rolfes, "Radar based material characterization at 145 GHz utilizing an ellipsoidal reflector," in *Proc. 49th Eur. Microw. Conf. (EuMC)*, Oct. 2019, pp. 527–530.

[7] S. Vogt, O. Garten, J. Jebramcik, J. Barowski, and I. Rolfes, "Asymptotic simulation methods as forward models in multilayer material characterization applications," in *IEEE MTT-S Int. Microw. Symp. Dig.*, Jul. 2019, pp. 109–111.

[8] J. Jebramcik, J. Barowski, and I. Rolfes, "Characterization of layered dielectric materials using ultra-wideband FMCW-radar measurements," in *Proc. Asia–Pacific Microw. Conf. (APMC)*, Nov. 2018.

[9] K. K. M. Chan, A. E.-C. Tan, L. Li, and K. Rambabu, "Material characterization of arbitrarily shaped dielectrics based on reflected pulse characteristics," *IEEE Trans. Microw. Theory Techn.*, vol. 63, no. 5, pp. 1700–1709, May 2015.

[10] E. Kemptner and S. Thurner, "Free space material characterization for microwave frequencies," in *Proc. 6th Eur. Conf. Antennas Propag. (EUCAP)*, Mar. 2012, pp. 3513–3515.

[11] K. Vera, B. Christian, C. van Driesten, and B. Erwin, "Retroreflective mmWave measurements to determine road surface characteristics," in *Proc. Kleinheubach Conf.*, Sep. 2019, pp. 1–4.

[12] V. Perez-Gracia, O. Caselles, J. Clapes, and S. Santos-Assuncao, "GPR building inspection: Examples of building structures assessed with ground penetrating radar," in *Proc. 9th Int. Workshop Adv. Ground Penetrating Radar (IWAGPR)*, Jun. 2017, pp. 1–4.

[13] Y. Hai-zhong, O. Yu-feng, and C. Hong, "Application of ground penetrating radar to inspect the metro tunnel," in *Proc. 14th Int. Conf. Ground Penetrating Radar (GPR)*, Jun. 2012, pp. 759–763.

[14] V. Pérez-Gracia, O. Caselles, J. Clapés, R. Osorio, J. A. Canas, and L. G. Pujades, "Radar exploration applied to historical buildings: A case study of the marques de Llió palace, in barcelona (Spain)," *Eng. Failure Anal.*, vol. 16, no. 4, pp. 1039–1050, Jun. 2009.

[15] X. Dérobert, J. Iaquinta, G. Klysz, and J.-P. Balayssac, "Use of capacitive and GPR techniques for the non-destructive evaluation of cover concrete," *NDT E Int.*, vol. 41, no. 1, pp. 44–52, Jan. 2008.

[16] L. Binda, L. Zanzi, M. Lualdi, and P. Condoleo, "The use of georadar to assess damage to a masonry bell tower in Cremona, Italy," *NDT E Int.*, vol. 38, no. 3, pp. 171–179, Apr. 2005.

[17] P. Zhang, Y. Li, Y. Zhao, and L. Guo, "Application and analysis on structure exploration of coal seam by mine ground penetrating radar," in *Proc. 14th Int. Conf. Ground Penetrating Radar (GPR)*, Jun. 2012, pp. 469–472.

[18] C. Baer, S. Gutierrez, J. Jebramcik, J. Barowski, F. Vega, and I. Rolfes, "Ground penetrating synthetic aperture radar imaging providing soil permittivity estimation," in *IEEE MTT-S Int. Microw. Symp. Dig.*, Jun. 2017, pp. 1367–1370.

[19] L. Fu, S. Liu, and L. Liu, "Numerical simulations and analysis for airborne ground penetrating radar," in *Proc. 14th Int. Conf. Ground Penetrating Radar (GPR)*, Jun. 2012, pp. 200–203.

[20] S. Lambot, E. C. Slob, I. van den Bosch, B. Stockbroeckx, and M. Vanclooster, "Modeling of ground-penetrating radar for accurate characterization of subsurface electric properties," *IEEE Trans. Geosci. Remote Sens.*, vol. 42, no. 11, pp. 2555–2568, Nov. 2004.

[21] L. Gurel and U. Oguz, "Three-dimensional FDTD modeling of a ground-penetrating radar," *IEEE Trans. Geosci. Remote Sens.*, vol. 38, no. 4, pp. 1513–1521, Jul. 2000.

[22] D. Goodman, "Ground-penetrating radar simulation in engineering and archaeology," *Geophysics*, vol. 59, no. 2, pp. 224–232, 1994.

[23] K. Yee, "Numerical solution of initial boundary value problems involving Maxwell's equations in isotropic media," *IEEE Trans. Antennas Propag.*, vol. 14, no. 3, pp. 302–307, May 1966.

[24] C. Statz and D. Plettemeier, "BETSi: An electromagnetic time-domain simulation tool for antennas and heterogeneous media in ground penetration radar and biomedical applications," in *Proc. Comput. Electromagn. Int. Workshop (CEM)*, Jun. 2017, pp. 37–38.

[25] L. Nagy, R. Dady, and A. Farkasvolgyi, "Algorithmic complexity of FDTD and ray tracing method for indoor propagation modelling," in *Proc. 3rd Eur. Conf. Antennas Propag.*, Mar. 2009, pp. 2262–2265.

[26] D. M. F. Gustrau, *EM Modeling of Antennas and RF Components for Wireless Communication Systems*. Berlin, Germany: Springer, 2006.

[27] A. Taflove, M. Piket-May, and S. Hagness, "FDTD-how complex a problem can we solve?" in *IEEE Antennas Propag. Soc. Int. Symp. Transmitting Waves Prog. Next Millennium Dig. Held Conjunct. (USNC/URSI)*, 2000, p. 1641.

[28] J. S. Araujo, R. O. Santos, C. L. S. S. Sobrinho, J. M. Rocha, L. A. Guedes, and R. Y. Kawasaki, "Analysis of antennas by FDTD method using parallel processing with MPI," in *IEEE MTT-S Int. Microw. Symp. Dig.*, 2003, pp. 1049–1054.

[29] J. M. Song and W. C. Chew, "Requirements scaling properties in large scale computing," in *IEEE Antennas Propag. Soc. Int. Symp. Dig. Antennas, Gateways Global Netw. Held Conjunct (USNC/URSI) Nat. Radio Sci. Meeting*, Jun. 1998, pp. 1518–1521.

[30] K. Zhang, L. L. Goddard, and J.-M. Jin, "Large-scale scattering analysis of arbitrary objects in a stratified medium," in *Proc. IEEE Int. Symp. Antennas Propag. USNC/URSI Nat. Radio Sci. Meeting*, Jul. 2018, pp. 1313–1314.

[31] D. B. Davidson, *Computational Electromagnetics for RF and Microwave Engineering*. Cambridge, U.K.: Cambridge Univ. Press, 2009.

[32] Y. M. Wu and W. C. Chew, "The modern high frequency methods for solving electromagnetic scattering problems," *Prog. Electromagn. Res.*, vol. 156, pp. 63–82, Jun. 2016.

[33] C. A. Balanis, *Advanced Engineering Electromagnetics*. Hoboken, NJ, USA: Wiley, 2012.

[34] Y. Berquin, A. Herique, W. Kofman, and E. Heggy, "Computing low-frequency radar surface echoes for planetary radar using Huygens-Fresnel's principle," *Radio Sci.*, vol. 50, no. 10, pp. 1097–1109, Oct. 2015.

[35] C. Statz, S. Hegler, and D. Plettemeier, "Method of iterative physical optics for the estimation of the scattering behavior of large layered dielectric bodies," in *Proc. IEEE Antennas Propag. Soc. Int. Symp. (APSURSI)*, Jul. 2013, pp. 1784–1785.

[36] D. Plettemeier *et al.*, "Numerical computation of radar echoes measured by MARSIS during phobos flybys," in *Proc. IEEE Radar Conf.*, May 2009, pp. 1–6.

[37] T.-Q. Fan, L.-X. Guo, B. Lv, and W. Liu, "An improved backward SBR-PO/PTD hybrid method for the backward scattering prediction of an electrically large target," *IEEE Antennas Wireless Propag. Lett.*, vol. 15, pp. 512–515, 2016.

[38] W.-W. Du, F. Wang, W.-X. Sheng, and X.-F. Ma, "Modeling and simulation of radar echo signal of aircraft targets with GRECO," in *Proc. 8th Int. Symp. Antennas, Propag. EM Theory*, 2008, pp. 859–862.

[39] F. Weinmann, "Ray tracing with PO/PTD for RCS modeling of large complex objects," *IEEE Trans. Antennas Propag.*, vol. 54, no. 6, pp. 1797–1806, Jun. 2006.

[40] D. Klement, J. Preissner, and V. Stein, "Special problems in applying the physical optics method for backscatter computations of complicated objects," *IEEE Trans. Antennas Propag.*, vol. AP-36, no. 2, pp. 228–237, Feb. 1988.

[41] M. Albani, G. Carluccio, and P. H. Pathak, "Uniform ray description for the PO scattering by vertices in curved surface with curvilinear edges and relatively general boundary conditions," *IEEE Trans. Antennas Propag.*, vol. 59, no. 5, pp. 1587–1596, May 2011.

[42] D. B. Davidson, "A review of important recent developments in full-wave CEM for RF and microwave engineering," in *Proc. 3rd Int. Conf. Comput. Electromagn. Appl. (ICCEA)*, 2004, p. 1.

[43] J. M. Rutherford and W. C. Chew, "Generalized solver hybridization using equivalence principle algorithm," *IEEE Trans. Antennas Propag.*, vol. 68, no. 3, pp. 2206–2212, Mar. 2020.

[44] S. Liu, B. Zou, and L. Zhang, "Hybrid method of FDTD/PO for EM scattering simulation of electrically large targets," in *Proc. IEEE Int. Symp. Antennas Propag. USNC-URSI Radio Sci. Meeting*, Jul. 2019, pp. 545–546.

[45] J. Chakarothai, K. Wake, S. Watanabe, A. Takuji, and T. Uno, "A hybrid MoM/FDTD method for exposure assessment of wireless power transfer systems," in *Proc. IEEE Int. Workshop Electromagn., Appl. Student Innov. Competition (iWEM)*, Aug. 2018, p. 1.

[46] G. Karagounis, D. De Zutter, and D. V. Ginste, "A hybrid MLFMM-UTD method for the solution of very large 2-D electromagnetic problems," *IEEE Trans. Antennas Propag.*, vol. 64, no. 1, pp. 224–234, Jan. 2016.

[47] Z.-L. Liu and C.-F. Wang, "Efficient iterative method of moments—Physical optics hybrid technique for electrically large objects," *IEEE Trans. Antennas Propag.*, vol. 60, no. 7, pp. 3520–3525, Jul. 2012.

[48] Y. Zhang, P. Sun, S.-W. Lu, and B. He, "Communication-zone field analysis of electronic-toll-collection system by hybrid FDTD-PO method," in *Proc. 12th Int. Conf. ITS Telecommun.*, Nov. 2012, pp. 706–709.

[49] T. Topa, A. Noga, and A. Karwowski, "FDTD/PO hybrid method for analysis of planar antennas radiating near large conducting objects," in *Proc. 21st Int. Conf. Radioelektronika*, Apr. 2011, pp. 1–3.

[50] L.-X. Yang, D.-B. Ge, and B. Wei, "FDTD/TDPO hybrid approach for analysis of the EM scattering of combinative objects," *Prog. Electromagn. Res.*, vol. 76, pp. 275–284, Jul. 2007.

[51] E.-X. Liu, E.-P. Li, and L.-W. Li, "Analysis of multilayer planar circuits by a hybrid method," *IEEE Microw. Wireless Compon. Lett.*, vol. 16, no. 2, pp. 66–68, Feb. 2006.

[52] A. Tzoulis and T. F. Eibert, "A hybrid FEBI-MLFMM-UTD method for numerical solutions of electromagnetic problems including arbitrarily shaped and electrically large objects," *IEEE Trans. Antennas Propag.*, vol. 53, no. 10, pp. 3358–3366, Oct. 2005.

[53] F. Le Bolzer, R. Gillard, J. Citerne, V. F. Hanna, and M. F. Wong, "An hybrid formulation combining FDTD and TDPO," in *Proc. IEEE Antennas Propag. Soc. Int. Symp. Dig. Antennas, Gateways Global Netw. Held Conjunct (USNC/URSI) Nat. Radio Sci. Meeting*, Jun. 1998, pp. 952–955.

[54] C. Statz, O. Garten, S. Hegler, and D. Plettemeier, "Implementation and hybridization of physical optics, born approximation, and ray tracing," in *Proc. Int. Workshop Comput., Electromagn., Mach. Intell. (CEMi)*, Nov. 2018, pp. 11–12.

[55] P. Pouliguen, R. Hémon, and J. Damiens, "Physical optics for large scale electromagnetic scattering problems," in *Proc. 4th Eur. Conf. Antennas Propag.*, Apr. 2010, pp. 1–4.

[56] J. S. Asvestas, "The physical optics method in electromagnetic scattering," *J. Math. Phys.*, vol. 21, no. 2, pp. 290–299, Feb. 1980.

[57] J. G. Meana, J. A. Martinez-Lorenzo, C. Rappaport, and F. Las-Heras, "Modified equivalent current approximation (MECA) applied to radio-electric coverage evaluation in rural scenarios," in *Proc. 4th Eur. Conf. Antennas Propag.*, Apr. 2010, pp. 1–4.

[58] C. T. Tai, "Direct integration of field equations," *Prog. Electromagn. Res.*, vol. 28, pp. 339–359, 2000, doi: 10.2528/PIER99101401.

[59] W. Franz, "Zur Formulierung des Huygensschen Prinzips," *Zeitschrift für Naturforschung A*, vol. 3, nos. 8–11, pp. 500–506, Nov. 1948.

[60] J. A. Stratton and L. J. Chu, "Diffraction theory of electromagnetic waves," *Phys. Rev.*, vol. 56, no. 1, p. 99, 1939.

[61] M. Arias *et al.*, "A physical optics simulator for dielectric bodies characterization using a multistatic radar," in *Proc. IEEE Int. Symp. Antennas Propag. USNC-URSI Radio Sci. Meeting*, Jul. 2019, pp. 819–820.

[62] W. C. Chew and Y. M. Wang, "Reconstruction of two-dimensional permittivity distribution using the distorted born iterative method," *IEEE Trans. Med. Imag.*, vol. 9, no. 2, pp. 218–225, Jun. 1990.

[63] Intel. *Embree*. Accessed: Feb. 20, 2020. [Online]. Available: https://www.embree.org/

[64] A. R. Diewald, "Farfield coupling of antennas in terms of s-parameters," in *Proc. German Microw. Conf. (GeMiC)*, Mar. 2016, pp. 92–95.

[65] N. Pohl and M. Gerding, "A dielectric lens-based antenna concept for high-precision industrial radar measurements at 24 GHz," in *Proc. 42nd Eur. Microw. Conf.*, Oct. 2012, pp. 405–408.

[66] (2018). *CST Microwave Studio*. [Online]. Available: https://www.3ds.com/products-services/simulia/products/cst-studio-suite

[67] *Simulation for Connectivity, Compatibility, and Radar | Altair Feko*. Accessed: Feb. 20, 2020. [Online]. Available: https://altairhyperworks.com/product/FEKO

[68] G. Gao and C. Torres-Verdin, "High-order generalized extended born approximation for electromagnetic scattering," *IEEE Trans. Antennas Propag.*, vol. 54, no. 4, pp. 1243–1256, Apr. 2006.

Orell Garten (Graduate Student Member, IEEE) received the Dipl.-Ing. degree in electrical engineering from Technische Universität Dresden, Dresden, Germany, in 2018. He is currently pursuing the Ph.D. degree in electrical engineering with Ruhr University Bochum, Bochum, Germany.

Since 2019, he has been with the Institute of Microwave Systems, Ruhr University Bochum, as a Research Assistant. His current research interests include computational electromagnetics, inverse problems, and high-performance computing.

Christoph Statz (Graduate Student Member, IEEE) received the Dipl.-Ing. degree in electrical engineering from Technische Universität Dresden, Dresden, Germany, in 2011, where he is currently pursuing the Ph.D. degree in electrical engineering.

Since 2011, he has been a Research Associate with the Chair for RF Engineering, Technische Universität Dresden. His current research interests include inverse problems, computational electrodynamics, high-frequency electromagnetic scattering, and radar sensing applications.

Steffen Gerling was born in Leer (Ostfriesland), Germany, in 1993. He received the M.Sc. degree in electrical engineering and information technology from Ruhr University Bochum, Bochum, Germany, in 2018, where he is currently pursuing the Ph.D. degree in electrical engineering.

Since 2018, he has been a Research Assistant with the Institute of Microwave Systems, Ruhr University Bochum. His current research interests include simulation methods and material characterization.

Jochen Jebramcik (Graduate Student Member, IEEE) was born in Essen, Germany, in 1987. He received the M.Sc. degree in electrical engineering and information technology from Ruhr University Bochum, Bochum, Germany, in 2014, where he is currently pursuing the Ph.D. degree in electrical engineering.

Since 2014, he has been with the Institute of Microwave Systems, Ruhr University Bochum, as a Research Assistant. His current research interests include simulation techniques, material characterization, and radar signal processing.

Dirk Plettemeier (Senior Member, IEEE) received the Ph.D. degree in electrical engineering from Ruhr-Universität Bochum, Bochum, Germany, in 2002.

Since 2011, he has been a Full Professor with the Chair for Radio frequency and Photonics Engineering, Technische Universität Dresden, Dresden, Germany. He is currently with the Center for Advancing Electronics Dresden and the Collaborative Research Center "Highly Adaptive Energy-Efficient Computing" where he is involved in electronics and energy-efficient computing systems for future applications. His current research interests include millimeter-wave and terahertz systems with a focus on antennas and chip-integrated applications, wave propagation, and remote sensing, as well as imaging solutions.

Jan Barowski (Senior Member, IEEE) was born in Bochum, Germany, in 1988. He received the B.Sc. and M.Sc. degrees in electrical engineering and the Dr.-Ing. degree in electrical engineering from Ruhr University Bochum, Bochum, Germany, in 2010, 2012, and 2017, respectively.

Since 2012, he has been with the Institute of Microwave Systems, headed by Ilona Rolfes, Ruhr University Bochum, as a Research Assistant. He is currently working as a Post-Doctoral Research Scientist with the Institute of Microwave Systems, Ruhr-University Bochum. His currents fields of research are concerned with radar signal processing, radar imaging, and material characterization techniques.

Ilona Rolfes (Member, IEEE) received the Dipl.-Ing. and Dr.-Ing. degrees in electrical engineering from Ruhr University Bochum, Bochum, Germany, in 1997 and 2002, respectively.

From 1997 to 2005, she was with the High Frequency Measurements Research Group, Ruhr University Bochum, as a Research Assistant. From 2005 to 2009, she was a Junior Professor with the Department of Electrical Engineering, Leibniz Universitaet Hannover, Hannover, Germany, where she became the Head of the Institute of Radio frequency and Microwave Engineering in 2006. Since 2010, she has been leading the Institute of Microwave Systems at Ruhr-University Bochum. Her fields of research concern high-frequency measurement methods for vector network analysis, material characterization, noise characterization of microwave devices, sensor principles for radar systems, and wireless solutions for communication systems.